applied sciences

MDPI

Article

FEA-Based Design Procedure for IPMSM and IM for a Hybrid Electric Vehicle

Emad Roshandel [1], Amin Mahmoudi [1,*], Wen L. Soong [2], Solmaz Kahourzade [3,*] and Nathan Kalisch [4]

[1] College of Science and Engineering, Flinders University, Adelaide 5042, Australia; emad.roshandel@flinders.edu.au
[2] School of Electrical and Mechanic Engineering, University of Adelaide, Adelaide 5005, Australia; wen.soong@adelaide.edu.au
[3] STEM, University of South Australia, Adelaide 5095, Australia
[4] Sovereign Propulsion Systems, Adelaide 5211, Australia; nathan@sovps.com.au
* Correspondence: amin.mahmoudi@flinders.edu.au (A.M.); solmaz.kahourzade@unisa.edu.au (S.K.)

Abstract: This paper describes the detailed design procedure of electric machines using finite element analysis (FEA). The proposed method uses the available findings from the literature and FEA results for the design procedure. In addition to electromagnetic analysis, thermal analysis is executed to examine the capability of the designed machines for handling the load in terms of thermal limits. It allows for considering the normal and overload performance of the electric machines during design. The proposed design procedure is used for designing a 100 kW induction machine (IM) and interior permanent magnet synchronous machine (IPMSM) for a parallel hybrid electric vehicle (HEV). The differences between the performance parameters of the studied machines are discussed, and the advantages and disadvantages of each design are highlighted. The designed machines are compared with commercially available electrical machines in terms of performance and power density. The comparison demonstrates that the developed machines can offer comparable performance to other designs.

Keywords: electric machine design; finite element analysis; hybrid electric vehicle; induction machine; PM machine; thermal analysis

Citation: Roshandel, E.; Mahmoudi, A.; Soong, W.L.; Kahourzade, S.; Kalisch, N. FEA-Based Design Procedure for IPMSM and IM for a Hybrid Electric Vehicle. *Appl. Sci.* **2024**, *14*, 10743. https://doi.org/10.3390/app142210743

Academic Editor: Jingyang Fang

Received: 6 September 2024
Revised: 31 October 2024
Accepted: 6 November 2024
Published: 20 November 2024

1. Introduction

The preparation of a suitable baseline electric machine design for a given specification is necessary to reduce the optimization variables and speed up the design and analysis process. The electromagnetic characteristics and temperature considerations are two important factors in this process [1].

This paper describes a detailed design procedure for the preparation of baseline designs for an interior permanent magnet synchronous machine (IPMSM) and induction machine (IM) for an example hybrid electric vehicle (HEV) application. The proposed design process benefits from the accuracy of 2D and 3D finite element analysis (FEA) in the design of the electric machines. The introduction is divided into two subsections, including a literature review section and a contributions section.

1.1. Background and Literature Review

Sizing equations [2], subdomain models (SDMs) [3], magnetic equivalent circuits (MECs) [4], and FEA [5] are common methods used for the electromagnetic design of electric machines.

Sizing equations are based on empirical equations developed by engineers. These equations are usually suitable for a specific geometry and material. Hence, they cannot predict electric machine performance parameters with a high accuracy, especially with a wide range of dimensions and machine sizes [6,7].

In SDMs, the Maxwell equations are solved in different parts of an electric machine. The obtained magnetic vector potentials are utilized to find the flux density and, hence, estimate the performance parameters [8–10]. In the past decade, researchers have proposed SDMs for induction machines [10], switched reluctance machines [9], and permanent magnet machines [8]. It was found that SDMs for IMs require slip and induced current modeling, those for SRMs require nonlinear magnetic saturation modeling, and those for PM motors require complex magnet interaction and torque ripple modeling. Researchers have demonstrated the accuracy of SDMs in the prediction of the performance parameters of electric machines. The implementation of SDMs is mathematically complex and needs a deep understanding of the electric machines being modeled. Hence, they have not become popular in engineering practice.

In MEC models, the electromagnetic reluctance and magnetic motive force (mmf) are obtained under a pole. Then, the MEC model is solved to find the mmf and flux in each region. This estimation enables a prediction of the performance parameters [11–13]. MECs are inaccurate if limited flux paths are investigated in the MEC model [11]. They can become more accurate by increasing the number of equivalent circuit elements, but this increases the computational burden [12,13].

FEA is one of the most precise tools for the prediction of electric machine performance parameters [14,15]. FEA is computationally expensive, which limits its application in designing machines for a given geometry [3]. On the other hand, the appearance of commercial and open-source software has led to the popularity of FEA.

The literature has described the design procedure for IPMSMs. The available literature discusses the optimization of IPMSMs with different objective functions to design a machine with the desired performance characteristics [16–19]. These studies normally use available commercialized geometries as the baseline. Some studies in the literature have optimized rotor or stator parameters to improve their performance based on the results of sensitivity analyses [20]. The effect of the winding configuration on improving the design has been another subject of study [21]. Rotor design and PM location and structure have become a popular method for improving IPMSM performance. The rotor of an IPMSM can include permanent magnets arranged in various patterns, including single-V-shape, double-V-shape, delta-shape, W-shape, U-shape, and spoke-type patterns. Choi et al. introduced an electromagnetic design procedure for a double-V-shaped IPMSM [22]. They used the results of a sensitivity analysis of different parameters of the stator and rotor to prepare a baseline design for their optimization study. The temperature effect, which is a crucial factor for design of electric machines, was ignored in Ref. [22].

A comprehensive comparative analysis was conducted in Ref. [23] to determine the optimum shape of an IPMSM rotor between single-V-shape, double-V-shape, and delta-shape configurations. The authors concluded that the single-V shape not only has the highest efficiency over a wide range of torques and speeds but also has a lower risk of demagnetization. A comparison of the V-shape, U-shape, and spoke-type IPMSMs revealed that the spoke type offered better performance at higher speeds, but it had the lowest torque density [24]. The larger saliency ratio of the V-shape configuration compared to the U shape allows for the production of a larger reluctance torque [25]. The V-shape design has been shown to be more robust against demagnetization [23,26].

The promising characteristics of V-shape PMs have encouraged researchers to optimize the dimensions and V angle in several studies [27]. The V angle has usually been investigated as a variable in iterative optimization studies [18,28]. In Ref. [29], it was shown that increasing the V angle can increase the torque in the constant torque region but reduces the maximum operating speed of the machine.

The design of line-start induction machines is well understood. The National Electrical Manufacturers Association (NEMA) and the International Electrotechnical Commission (IEC) have standardized IM dimensions and power ratings for line-start applications and the required geometry, number of rotor and stator slots, and slot types are specified to achieve the required performance while meeting the thermal and mechanical constraints [30,31].

The literature has shown that IMs can be a suitable choice for the propulsion systems of EVs and HEVs. They offer comparable efficiency with PMSMs in the field weakening region, and are of lower cost due to the absence of PM material in their rotor, but generally have a lower power density.

A large number of papers have discussed the design of IMs based on the sizing equations [32]. These methods are not useful for the design of IMs in EVs because they are only optimal for operation at a single operating point. Some literature employs sizing equations in population-based iterative optimization studies. However, these studies cannot produce a true optimal design because the sizing equations used are not reliable over a wide range of dimensions and loading levels [2].

The number and shape of the rotor bars play an important role in the performance parameters of IMs. Different optimization problems have been defined to achieve desired outputs such as high torque or efficiency [33,34]. An optimization study for an axial-flux IM was performed in Refs. [6,35]. Although optimal designs were determined, the effect of slot shape on the performance parameters has not been discussed.

In Ref. [30], the authors showed that the optimal number of rotor bars depends on the type of the supply (line start or inverter driven) and the number of pole pairs. Round rotor slots reduce the vibration and noise as compared to rectangular slots [36]. It has been shown that deeper and wider rotor bars increase the efficiency while improved starting and power factor are obtained by shorter bars [37]. Thirteen different shapes of rotor slots was studied in Ref. [38] to find the optimal shape of the bars which offer the highest efficiency and starting torque. These studies discussed the characteristics for a particular operating point and do not consider the performance analysis for a wide range of torque and speeds. Moreover, these papers just describe the effect of their considered variables on the case studies and do not cover the complete procedure to develop a baseline design.

The aforementioned design processes ignore the temperature effect or assume some constant values to guarantee the feasibility of the design in terms of the thermal stress [16,35]. For instance, a constant value of current density, whose value depends on the cooling method used, is often assumed to determine the slot area [39,40].

Considering the above limitations of the design procedures in the literature, there is a lack of a systematic design procedure for preparation of a baseline design for PMSMs and IMs.

1.2. Contributions and Significance

The main contribution of this paper includes a thorough exploration of approaches for the design of electrical machines utilizing finite element analysis tools. It integrates electromagnetic and thermal analyses to assess the overload performance and transient temperature variation for IMs and IPMSMs for application in HEVs, which has received limited attention in the literature. While the core concepts presented are known, this study contributes to advancements in the design of electrical machines tailored to specific operational conditions, rendering it of relevance and practical significance. It highlights the trade-offs between size and performance regarding the inclusion of overload capability and temperature consideration. It also includes a comprehensive literature review, elucidating the unique aspects of the proposed approach compared to prior methodologies, as well as a comparative analysis of the performance parameters of two machine designs against well-established commercial counterparts. The paper goes beyond the explanation of the traditional electromagnetic design methods by addressing how different machine types handle the overload conditions and critically analyzing their temperature limitations. The paper clarifies the difference between the torque capability of both machines by consideration of the temperature and overload capability limits. Other contributions include analysis of the impact of the use of deep V-shape PMs in achieving high torque density with low torque ripple and the analysis of the effect of the number of rotor bars on the performance parameters of the IM.

2. Design Specifications for the HEV

The design of two 100 kW electric machines for the propulsion system of a heavy hybrid electric vehicle with the requirements tabulated in Table 1 is the subject of the study in this paper. The investigated HEV has a parallel hybrid electric drive with two identical 100 kW motor/generators and a mechanical clutch [41] (see Figure 1). The clutch allows pure electric vehicle operation. It also allows the engine to run the generator machine when the vehicle is stationary to provide auxiliary power to external loads.

Table 1. The electric machine requirements for the HEV, reprinted with permission from IEEE [41].

Rated speed	2800 rpm	Maximum speed	3200 rpm
Rated power	100 kW	Overload capability	2 pu power for 30 s
Coolant flow rate	40 L/min max	Coolant	80 °C mixture of 50/50 water/glycol
Axial length	150 mm	Outer diameter	400 mm

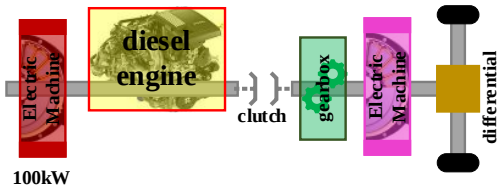

Figure 1. The schematic of the proposed HEV transmission system, reprinted with permission from IEEE.

The rated operating speed of the engine is 2800 rpm and its maximum speed is 3200 rpm. The generator must produce 100 kW during continuous operation and have the capability of generating 200 kW for 30 s during overload operation. The cooling system delivers an 80 °C mixture of water/glycol to the electric machine with a maximum flow rate of 40 L/min. The maximum machine diameter is 550 mm and the minimization of the axial length is another requirement of the design.

2.1. Requirements of the Direct Drive Electric Machines

Table 2 lists the selected materials for the designed electric machines. The windings of both machines use copper and a standard conductivity of 58 MS/m at 80 °C is assumed. Class F insulation is used, which allows for operation at hotspot temperatures of up to 155 °C. Considering the high temperature of the available coolant (80 °C), samarium–cobalt (Sm_2Co_{17}) magnets are used to reduce the risk of demagnetization. This has a magnetic flux remanence of 1.13 T at 20 °C.

Table 2. The selected materials for the electric machines.

	Stator Windings	**Rotor and Stator Lamination Material**	**PM**	**Cage**
IM	Copper with class F insulation	M250-35A	-	Copper
IPMSM	Copper with class F insulation	M250-35A	Sm_2Co_{17}	-

The IM cage is normally made of either copper or aluminum. Although cheaper, the conductivity of aluminum (33.3×10^7 S/m) is lower than that of copper (5.80×10^7 S/m) which leads to increased cage losses. Hence, for this application, a copper cage which offers higher efficiency is selected.

2.2. Thermal Model and Cooling System

Electric machine thermal analysis is usually performed using lumped equivalent circuits or 2D/3D finite element analysis [15,42,43]. The literature shows that these models can predict the average temperature of the different parts in an electric machine with acceptable accuracy. The Motor-CAD 2022 R2 software is a thermal analysis package which employs both lumped circuit and FEA modeling. The boundary conditions and material characteristics are adjusted based on empirical equations [44,45]. This paper uses Motor-CAD for modeling of the proposed cooling system.

Similar cooling jackets with spiral cooling channels are assumed for both the IM and IPMSM stators as shown in Figure 2. The literature shows that this provides good heat removal from the stator and produces a reasonably uniform temperature distribution [46]. The height and width of the water channels are 5 mm. The coolant information was presented earlier in Table 1.

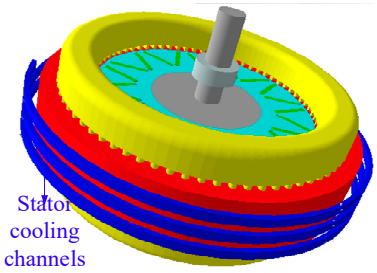

Figure 2. The schematic of the proposed spiral cooling system for the stators of both machines.

The rotor bars of induction machines have losses which are normally comparable in magnitude to the stator winding losses and so require a suitable cooling system [47]. In this paper, a spiral groove is assumed to be embedded into the IM shaft to remove these rotor losses [1,48].

3. Design Procedure

This section describes the design procedure used to design the IPMSM and IM with the maximum power rating within the given geometry and thermal limits.

3.1. IPMSM Design Procedure

Figure 3 shows the flowchart of the proposed design procedure for the IPMSM. The number of poles and stator slots are selected in the first step.

For the number of poles, a higher number of poles reduces the required stator and rotor yoke thicknesses and hence achieves higher torque density. However, increasing the number of poles leads to increasing the operating frequency and hence core losses of the machine for a given operating speed. For reasonable lamination thicknesses, the operating frequency is normally selected in the range of 250 Hz to 500 Hz [47,49,50].

For the stator slots, it is preferable to use a larger number of narrower slots to improve the stator winding cooling. This is limited by the mechanical strength of the stator laminations and achieving reasonable winding fill factors for the narrow slots. The number of slots is selected based on observations of similar commercial designs to guarantee the feasibility of the lamination design.

The literature shows that IPMSMs with a number of slots per pole per phase (SPP) of two introduces lower torque ripple and cogging torque compared to an SPP of one and fractional values [51]. This SPP value also has low total harmonic distortion of the back-emf. Thus, the numbers of poles and slots are selected to give a value of SPP of two.

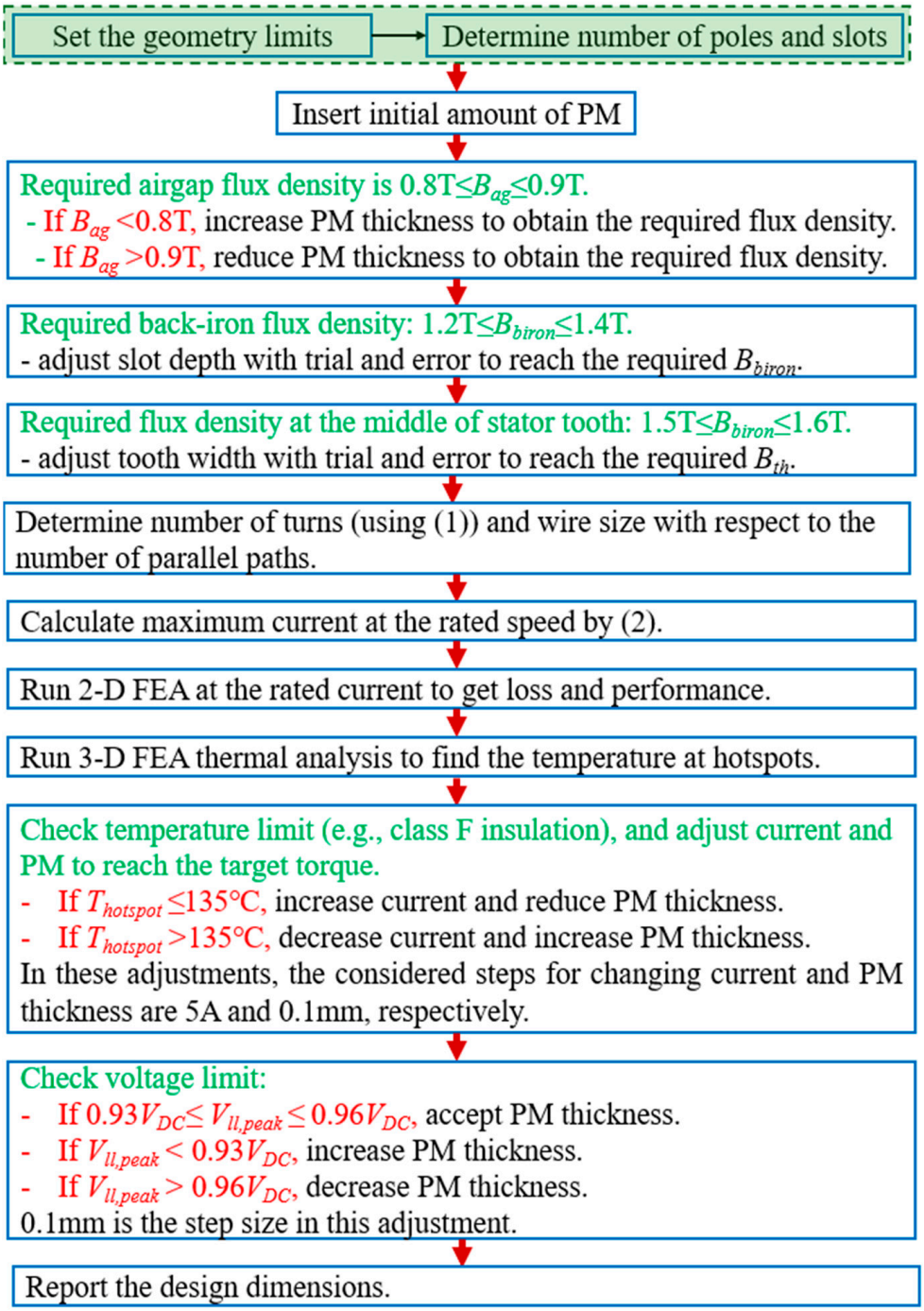

Figure 3. The design flowchart of the studied 100 kW interior permanent magnet synchronous machine.

The generated torque is proportional to the product of the airgap area, airgap diameter, magnetic loading, and electric loading. Increasing the airgap diameter also increases the airgap area but reduces the available stator slot cross-sectional area and hence the electric loading. In most IPMSMs with normal axial length to outer diameter aspect ratios, like the IPMSMs studied in Refs. [16,52,53], the ratio of the inner to stator outer diameter is in the range 0.6 to 0.7. When the available axial length is limited, it is reasonable to increase this ratio to 0.7 or higher [52].

After the determination of the machine geometry and number of slots/poles, the stator slot dimensions and PM volume should be found. An initial magnet design with a pole pitch of 80% and thickness of 6 mm was used. The literature shows that optimum IPMSM

designs with the laminated steel generally have a stator back-iron flux density of 1.2–1.4 T at no load [54]. So, the average airgap flux density (B_{ag}) is checked to be in the range of 0.8 T to 0.9 T, and the PM amount is adjusted, if necessary, to achieve this.

After the desired value of B_{ag} is obtained, the stator back-iron thickness is adjusted to reach a flux density of 1.2 T to 1.4 T in the back-iron. Then, the stator teeth width is adjusted to obtain a flux density of 1.5 T to 1.6 T in the teeth [55]. The stator teeth should be roughly 50% to 66% of the slot pitch at the mean stator slot diameter.

The voltage equation presented in (1) is used to determine the number of turns per phase (N_{ph}). In this equation, A and B_{ag} are the airgap area of each pole and the airgap flux density. The frequency of the operation at the rated speed is shown by f.

$$E = 4.44 B_{ag} A N_{ph} f \tag{1}$$

The stator winding copper wire diameter is chosen to be about 1 mm which is easier for winding. Assuming a copper slot fill factor of 0.45, the number of parallel branches for the obtained number of turns is then determined.

High-power PMSMs normally offer a high efficiency and power factor in their constant torque region. It is assumed that the product of power factor ($\cos\varphi$) and efficiency (η) for this machine should be around 0.95 [56]. The following equation can be used to find the machine current (I_s) for generation of maximum torque:

$$I_s = \frac{P_{out}}{\sqrt{3} V_{ll} \eta \cos(\varphi)} \tag{2}$$

In Equation (2), P_{out} and V_{ll} are the output power and rms line voltage at the maximum speed at the end of the constant torque region.

Standard Class F insulation is used, which allows operating temperatures of 145 °C with a hotspot temperature of 155 °C. The value of rated current is found as the current which produces this hotspot temperature limit in the windings [57]. From the value of rated current, the required PM volume can be found by means of a sensitivity analysis in FEA.

Considering the advantages of the V-shape PM topology discussed in the Introduction section, this configuration is selected for the design. To optimize its value, the V angle is changed from 180° to 60° and the airgap flux density is monitored while the PM volume is kept roughly constant. The FEA results indicate that the 60° design provides an airgap flux density that is about 25% higher than the other two designs. This increased flux density presents an opportunity to reduce the number of turns in the machine, thereby achieving lower copper losses. Figure 4 shows the results for the three V angles. The back-emf waveform of the 60° design is more sinusoidal than the other two designs which gives a higher power factor. The total harmonic distortion (THD) of the back-emf for the 60° design is 1.4% while for the 180° and 150° designs it is 7.5% and 5%, respectively. Although the cogging torque of the machine with the 60° angle is larger than with the 180° angle (i.e., 15 Nm peak vs. 3 Nm peak), its percentage torque ripple at the rated point is 10% which is 7.3% smaller than the 180° design and 3.7% smaller than the 150° design.

The higher average torque, lower ripple torque, and lower THD of the 60° design make it superior in terms of its electromagnetic performance. However, because of the larger width of the PMs in the 60° design, it has a smaller inner diameter and higher rotor weight. The short circuit current of the 60° design is also higher than the two other designs, which could increase the risk of demagnetization.

As shown in Figure 4, the rated currents were found by considering the voltage and winding thermal constraints. These are affected by the number of turns and the airgap flux density. The 60° design has the highest rated current, followed by the 180° design.

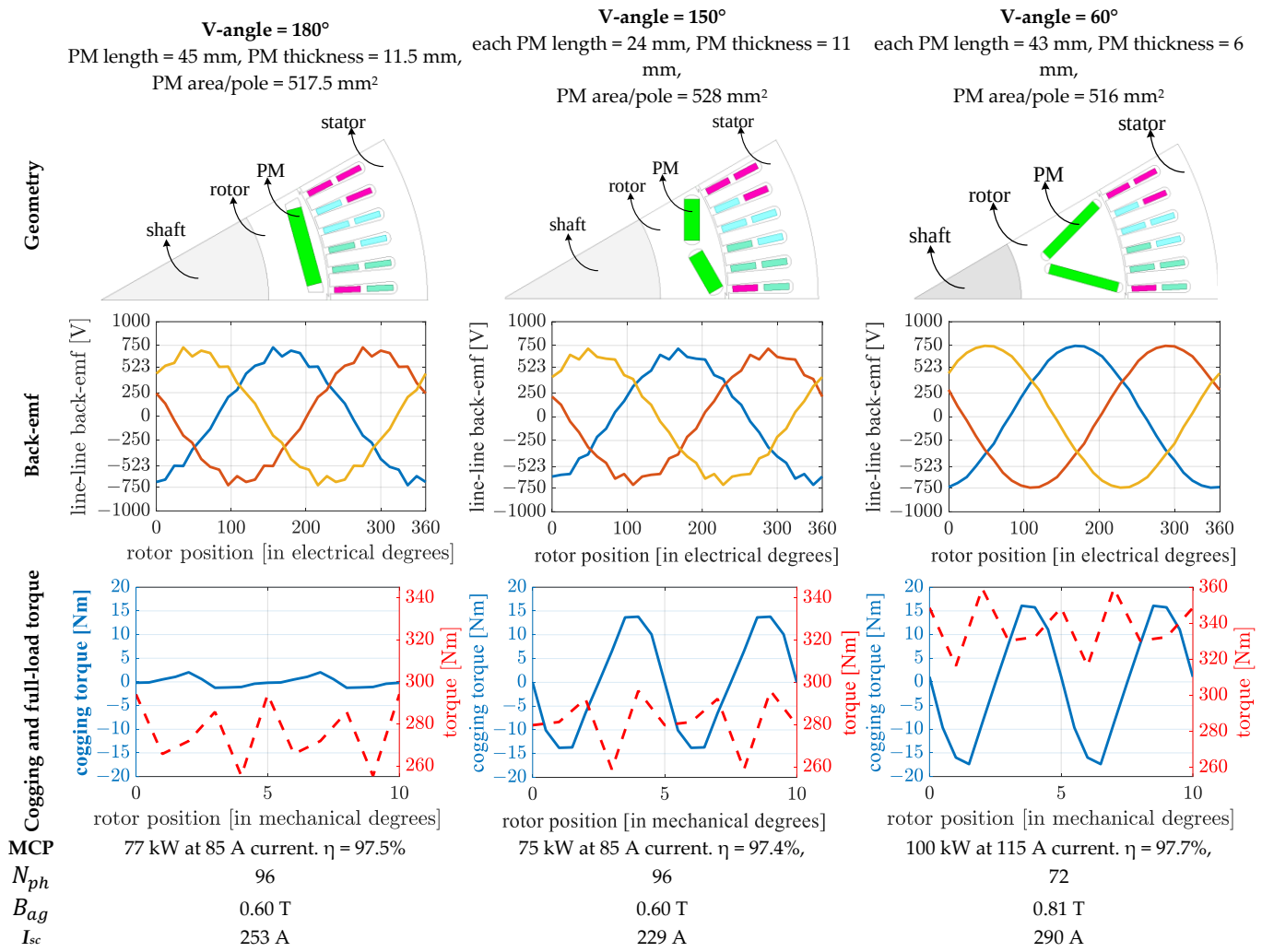

Figure 4. Two-dimensional FEA results of the studied PMSM V-shape rotors for different rotor magnet angles. The maximum continuous power (MCP) is reported @2800 rpm with Class F temperature rise. I_{sc} is the short circuit current.

It should be highlighted that structural, vibration, and noise analysis are other factors which can be studied with consideration of the different PM angles to determine the optimum design. These analyses are out of the scope of this paper.

Bar graphs of the stacked losses as a fraction of the input power for the three designs are presented in Figure 5. This shows that the majority of losses are due to the stator copper losses, followed by stator iron losses, and there are only a small amount of rotor iron and magnet losses. It should be highlighted that the number of turns per phase of the V-60 is about 25% less than the other designs. This reduction enables the use of a conductor with a larger cross-sectional area, which in turn helps achieve lower resistance. Consequently, the stator resistance of the V-60 design is 0.036 Ω, compared to 0.065 Ω in the other designs. Although the winding resistance of V-60 is lower, its copper losses are approximately equal to the other designs because of its higher rated current.

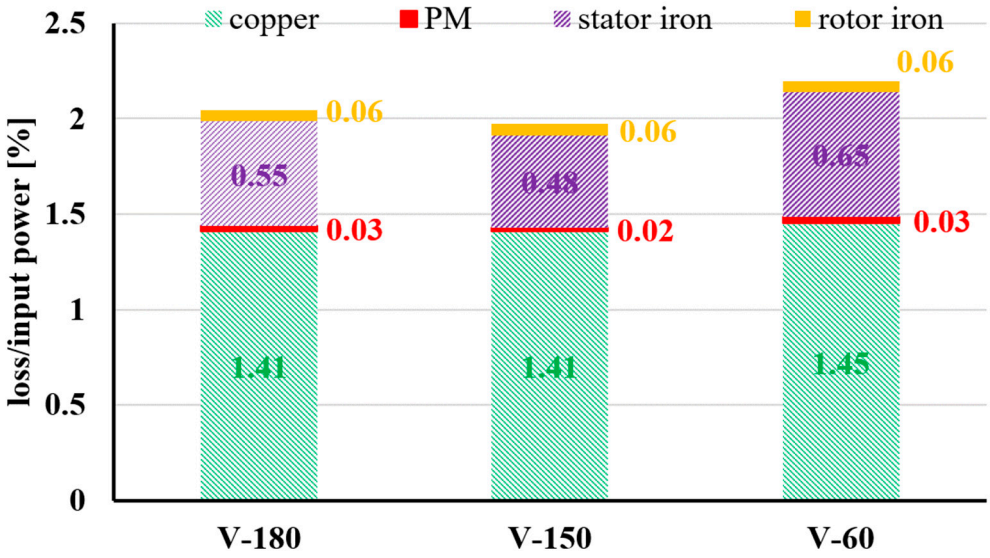

Figure 5. Stacked bar graphs of the losses of the three PMSM designs obtained from 2D FEA.

3.2. IM Design Procedure

As shown in Figure 6, the design process for the IM starts with the determination of the number of poles and slots based on the same principles as for the IPMSM design. The number of turns is found using Equation (1) with the assumption of 0.7 T for the airgap flux density.

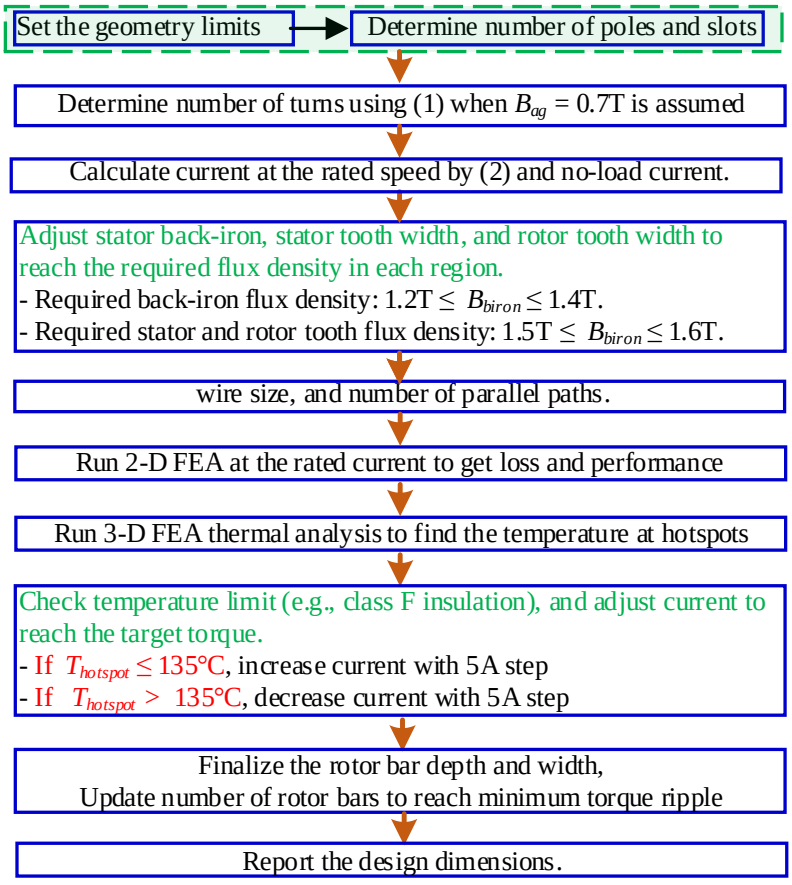

Figure 6. The proposed step-by-step design process for the induction machine design.

According to [30], it is reasonable to select the number of rotor bars (N_R) in the following range:

$$0.5N_S \leq N_R \leq 1.5N_S, \quad (3)$$

where N_S is the number of stator slots. The results of the analysis in Ref. [58] demonstrates that the torque ripple is zero but the machine cannot be line started when $N_S = N_R$. Because the line-start operation of the IM is not an important criterion for the considered HEV, the initial value of N_R is assumed to be equal to the stator slots ($N_R = N_S$). An arbitrary, but reasonable, value (i.e., 10–15% of the rotor radius) is assumed for the bar depth and their width is chosen to be roughly equal to the stator slot width.

The power factor of induction machines is normally in the range of 0.7 to 0.9. Based on this it was assumed that $\eta \cos(\varphi) = 0.65$. Considering this value, a possible rated current for the IM is calculated at this stage. Normally, the no-load current in IMs is 40% to 60% of the rated current. It is assumed that the no-load current in this design is 50% of the rated current. The calculated no-load current is injected into the winding in 2D FEA when the rotor is rotated at the no-load speed. The no-load simulation is executed for different slot heights and widths to achieve the desired back-iron and tooth flux densities in both the rotor and stator. The desired values have been indicated in Figure 6 which have been selected based on the information in Refs. [55,59]. The rotor tooth width is kept 1 mm less than the stator tooth width during the analysis, based on the e-mobility IM design described in Ref. [48]. At this stage the rotor slot height is kept constant.

In published IM designs for EVs and HEVs, the IM typically operates at 0.1–1% slip over a wide range of torque and speed. Hence, the rotor of the machine is rotated with 0.5% slip when a current-driven IM is simulated using 2D FEA at rated frequency. The amplitude of the current is increased to reach the limits of the Class F insulation. The stator voltage is checked to ensure that the machine does not exceed the DC-link voltage limit. This current is selected as the rated current of the designed IM.

The dimensions of the rotor bars are then optimized to improve performance. Increasing the rotor bar width and depth reduces the rotor resistance and hence losses and can also produce less torque ripple. On the other hand, the increase in the bar width reduces the rotor tooth cross-sectional area which can lead to saturation and hence torque reduction. Also, the increase in the bar depth leads to an increase in the length of the flux path and, consequently, possible additional saturation and core loss. Hence, the width and depth of the rotor bars are varied to find the optimum value through the FEA simulations.

After the rotor bar dimensions have been optimized for a given number of rotor bars, the number of rotor bars, which gives minimum torque ripple, is optimized keeping the bar depth and total rotor bar cross-sectional area constant.

4. Design of the IPMSM and IM Using the Proposed Procedure

4.1. Available Space for Design

The geometry requirements, presented in Table 1, are a challenge of this design. Given the maximum of 400 mm for the housing outer diameter (OD), a value of 370 mm is chosen for the stator OD to allow a 15 mm radial thickness for the housing with 10 mm spiral cooling channels. Given the 150 mm maximum axial length requirement, it is assumed that the housing thickness occupies 2.5 mm of axial length on each side. The end-winding length reduces the available axial space for the machine. Based on the chosen number of poles, slots, and winding design, which will be explained later, a 3D printed stator was provided for the coil winder to perform a sample winding to estimate the length of end winding. This was found to be about 40 mm. Thus, the maximum machine stack length would be only 65 mm.

4.2. IPMSM Design Example

The number of poles and number of slots should be determined at the first step. Given 3200 rpm as the maximum speed of the machine, the number of poles can be a value in the range of 10 to 20 poles based on the stator fundamental frequency in the range 250 to 500 Hz.

Based on scaling of a commercial line-start induction machine design to the proposed 370 mm stator outer diameter, 72 slots were chosen for the stator. The selection of a value of slot per pole per phase (SPP) of 2, based on torque ripple and THD considerations, with 72 slots determines the machine number of poles which is equal to 12.

The inner to outer stator diameter ratio of 0.6 to 0.8 is a typical value for electrical machines (for instance, the IM in the Tesla model S used 0.6 [59]), and a value of 0.7 was used. Given 370 mm for the outer diameter, the inner diameter will be equal to 259 mm. Given the dimensions of the machine and the high operating temperatures, a 1 mm airgap length is used.

The stator yoke and tooth thicknesses are obtained using the optimization procedure described in the previous section. The resultant yoke and tooth thicknesses are 17 mm and 7.3 mm, respectively.

Based on the specifications, the maximum DC-link voltage of the machine is 750 V which limits the maximum rms phase voltage (E) to 286 V. Therefore, the number of series turns (N) is found using Equation (1) to be 72 turns per phase.

The 60° V-shaped topology is selected for the rotor based on the analysis in the previous section. As explained, the amount of PM material is adjusted to reach the 0.85 T airgap flux density. The rated current is then calculated by Equation (2). The machine's thermal performance is examined and if the temperatures are too high, the current is reduced, and the PM volume is increased if necessary to reach the expected performance within the voltage limit.

The cross-section of the final design of the 100 kW IPMSM was presented earlier in Figure 4 (rightmost design) and Table 3 summarizes its dimensions.

Table 3. Dimensions of the designed IPMSM.

Parameter	Value	Parameter	Value
Outer diameter [mm]	370	Inner diameter [mm]	260
Slot depth [mm]	38	Tooth width [mm]	7.3
PM thickness [mm]	6	PM length [mm]	43
Length of air barriers [mm]	2	Airgap length [mm]	1
Shaft diameter [mm]	130	Stator stack length [mm]	65
Winding end-winding length [mm]	40	Number of poles	12
Number of turns per slot	6	Number of slots	72

4.3. IM Design Example

The geometry requirements are also applied for the design of the IM and the same number of slots and poles, and ratio of inner to outer stator diameters was chosen.

Considering a maximum DC-link voltage of 750 V, the number of turns per slot are calculated using Equation (1) for a 0.7 T average airgap flux density and a 280 Hz operating frequency. Considering these values, the obtained number of turns per slot is 6 turns.

To find the stator slot and yoke dimensions, the initial value of the number of rotor slots N_R is assumed to be equal to the stator slots ($N_R = 72$). The process described in the design procedure was used to obtain the stator tooth width and back-iron thickness as 7 mm and 17 mm, respectively, and then the optimum rotor dimensions as the rotor tooth width and bar depth as 5.7 mm and 24.5 mm, respectively.

Figure 7 shows the effect of changing the number of rotor bars on the rated performance of the IM while keeping the total rotor slot area constant. Figure 7a shows that the

torque ripple becomes larger when the difference between the number of rotor and stator slots is increased. The minimum torque ripple occurs with 72 rotor bars which is similar to the conclusion of the previous work conducted by Joksimovic [30,58]. As shown in Figure 7b the generated torque, output power, and power factor are increased by increasing the number of rotor bars because the airgap flux is found to increase. The higher airgap flux does increase the core loss and consequently the iron temperature by a small amount. Figure 7c shows that with a larger number of rotor bars (i.e., 78 to 92 bars) the rotor iron temperature is slightly (about 1 °C) higher. The stacked loss of the machine with different numbers of rotor bars is presented in Figure 8. As expected, the loss is increased slightly by the increase in the number of rotor bars. The 2D FEA results show that the rotor core loss increased by about 1% from 64 to 92 bars. These results show that the design with 78 bars offers an acceptable performance with small torque ripple, and it was selected. The geometry and cross-section of the proposed machine are presented in Table 4 and Figure 9, respectively.

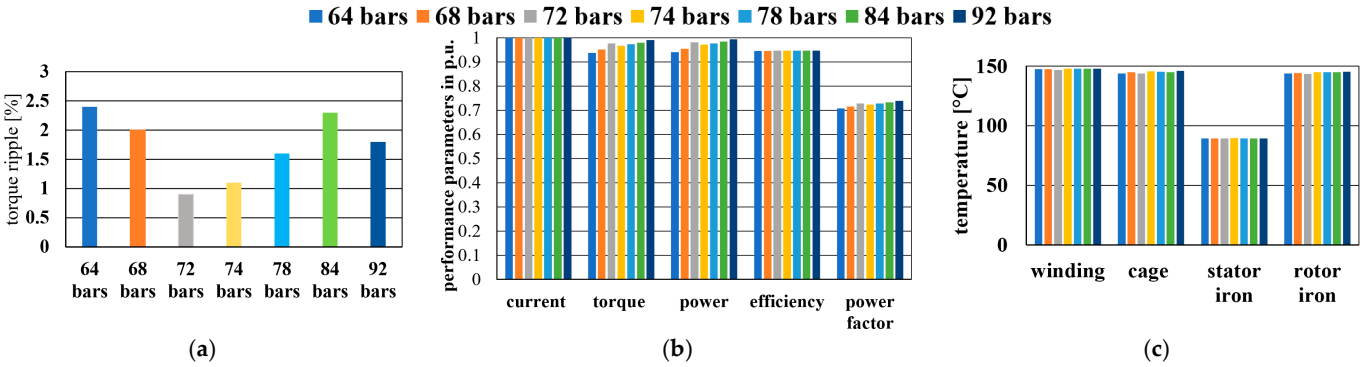

Figure 7. Effect of the number of rotor bars: (**a**) 2D FEA results of torque ripple at rated torque, (**b**) 2D FEA results of performance parameters, (**c**) 3D FEA results of hot spot temperatures. The current, torque, and output power are per unit based on their rated values which are 120 A, 260 Nm, and 80 kW, respectively.

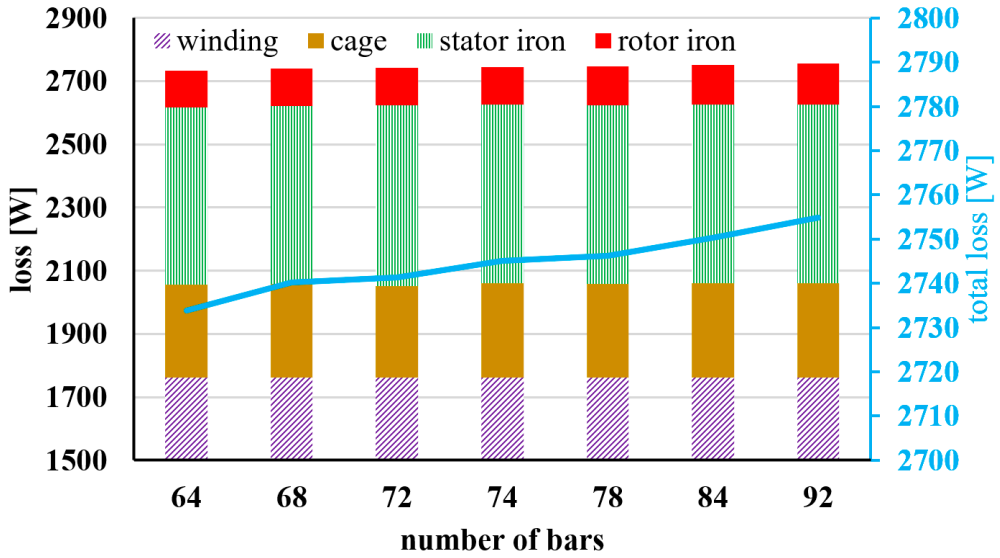

Figure 8. Two-dimensional FEA results of the IM loss breakdown for different numbers of rotor bars.

Table 4. The dimensions of the designed IM.

Parameter	Value	Parameter	Value
Outer diameter [mm]	370	Inner diameter [mm]	260
Slot depth [mm]	42	Stator tooth width [mm]	6.9
Rotor bar depth [mm]	24.5	Rotor tooth width [mm]	5.3
Airgap length [mm]	0.5	Shaft diameter [mm]	170
Winding end-winding length [mm]	40	Stator stack length [mm]	65
Number of rotor bars	78	Number of poles	12
Number of stator slots	72	Number of turns per slot	6

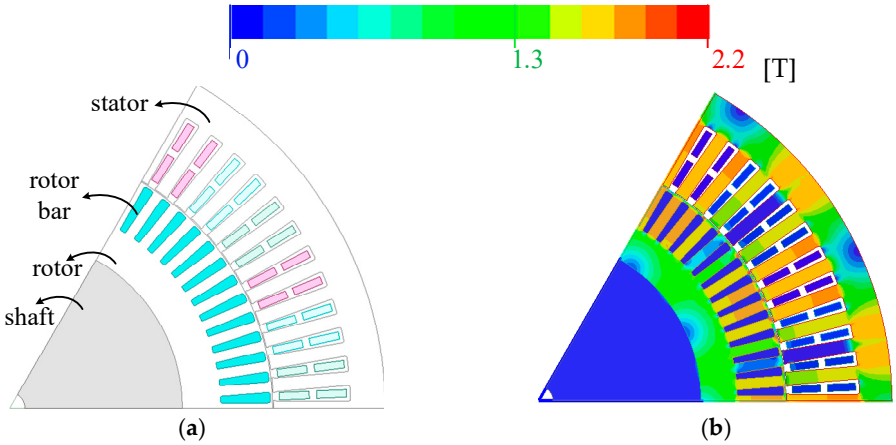

Figure 9. (**a**) Cross-section of the designed induction machine, (**b**) flux density distribution in the full-load operating condition.

5. Simulation Results and Discussion

In this section, the finite element analysis (FEA) performance parameters of these machines are compared over a wide range of torques and speeds in the required operation region and overload condition. Finally, the proposed design procedure is used to design these machines with different numbers of poles to study the effect of the selection of pole numbers.

The FEA models for both the induction (IM) and permanent magnet (PM) models were developed and analyzed on a computer equipped with a 13th Gen Intel Core i9-13980HX CPU and 32 GB of RAM. The IM model consists of 4185 mesh nodes and 8195 mesh elements, while the PM model includes 3208 mesh nodes and 6132 mesh elements. In both models, the maximum element length is 0.4 mm. The FEA for a single operating point requires 57 s for the IM model and 42 s for the PM model. Additionally, the thermal analysis at a single operating point takes 7 s for the IM model and 4 s for the PM model.

5.1. Performance Parameters

Although the machines have been designed for operation as generators in the considered HEV, the performance parameters in this section are provided for both motoring and generating conditions to demonstrate the differences.

The power, efficiency, and power factor maps of the designed IPMSM and IM are discussed in this section. The calculation procedure of these has been described in Ref. [60]. Figure 10 compares the output rated power of both machines. It is seen that the IPMSM offers a higher power (larger torque) capability at lower speeds. The maximum power of the IPMSM is 103 kW while the IM is limited to 75 kW. It should be highlighted that the induction machine offers 81 kW during generating operation at the rated speed which is

6 kW greater than the power in the same motoring condition. The maximum output power of the IPMSM in motoring mode is 2 kW greater than its output generating power.

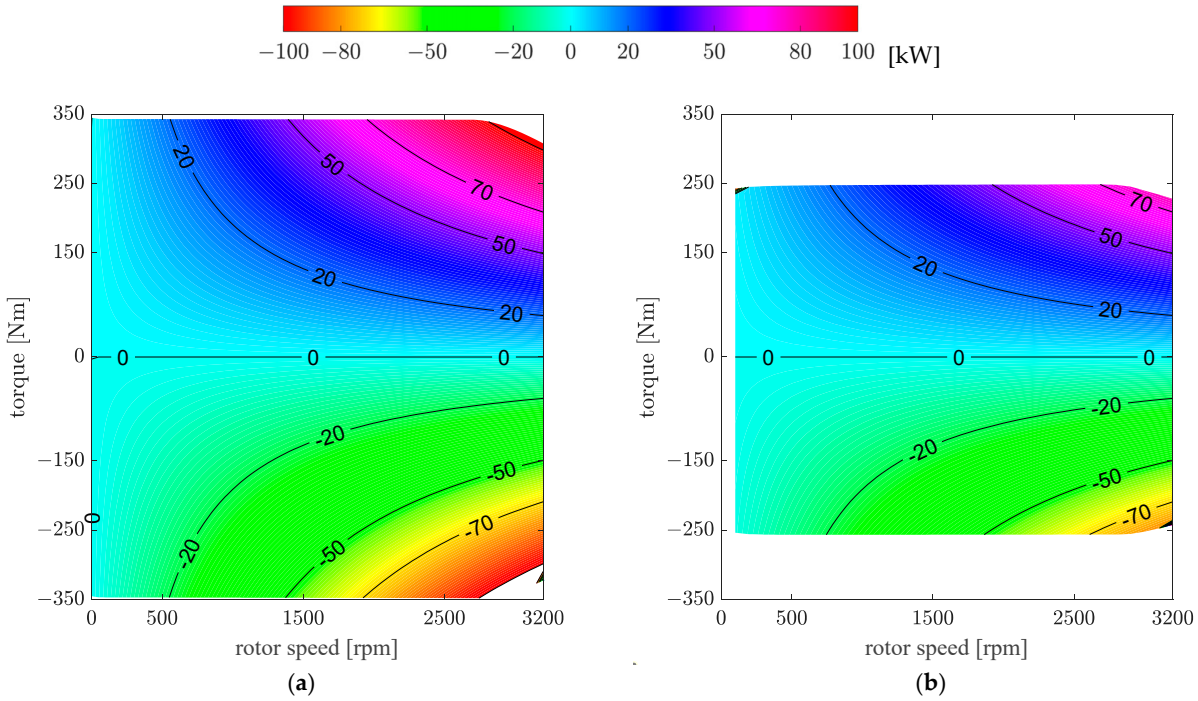

Figure 10. Two-dimensional FEA output power results: (**a**) IPMSM, (**b**) IM.

The efficiency maps of the designed machines are compared in Figure 11. This shows the efficiency of the IPMSM is at least 2% greater than the IM in both motoring and generating modes. Note that at lower speeds this difference reaches 7%, which is significant. In addition, the high-efficiency region for the IPMSM covers a larger area than for the IM.

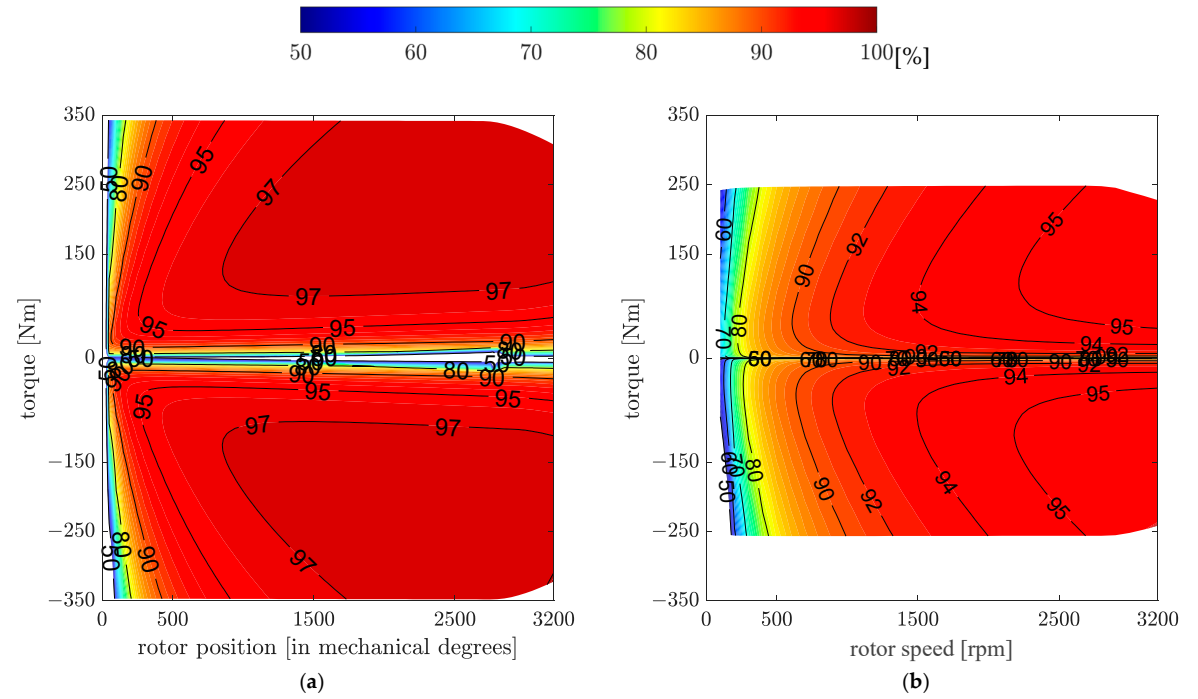

Figure 11. Two-dimensional FEA efficiency map results: (**a**) IPMSM, (**b**) IM.

Table 5 compares the electromagnetic weight, power, and efficiency. The IM is approximately 10 kg heavier than the IPMSM because of the copper rotor cage. The power densities of the IPMSM and IM are about 2.1 kW/kg and 1.4 kW/kg, respectively.

Table 5. Comparison of the IPMSM and IM.

	Weight [kg]				Power [kW]		Efficiency [%]	
	Winding	**Cage**	**Iron**	**PM**	**Rated**	**Peak**	**Rated**	**Peak**
IPMSM	12.0	-	34.4	3.0	103	206	97	91
IM	12.0	13.1	31.4	-	81	162	95	92

The comparison of the power factor of the two electric machines in Figure 12 demonstrates the larger power factor of the IPMSM at most of the operating points. At larger torques this difference is about 37%.

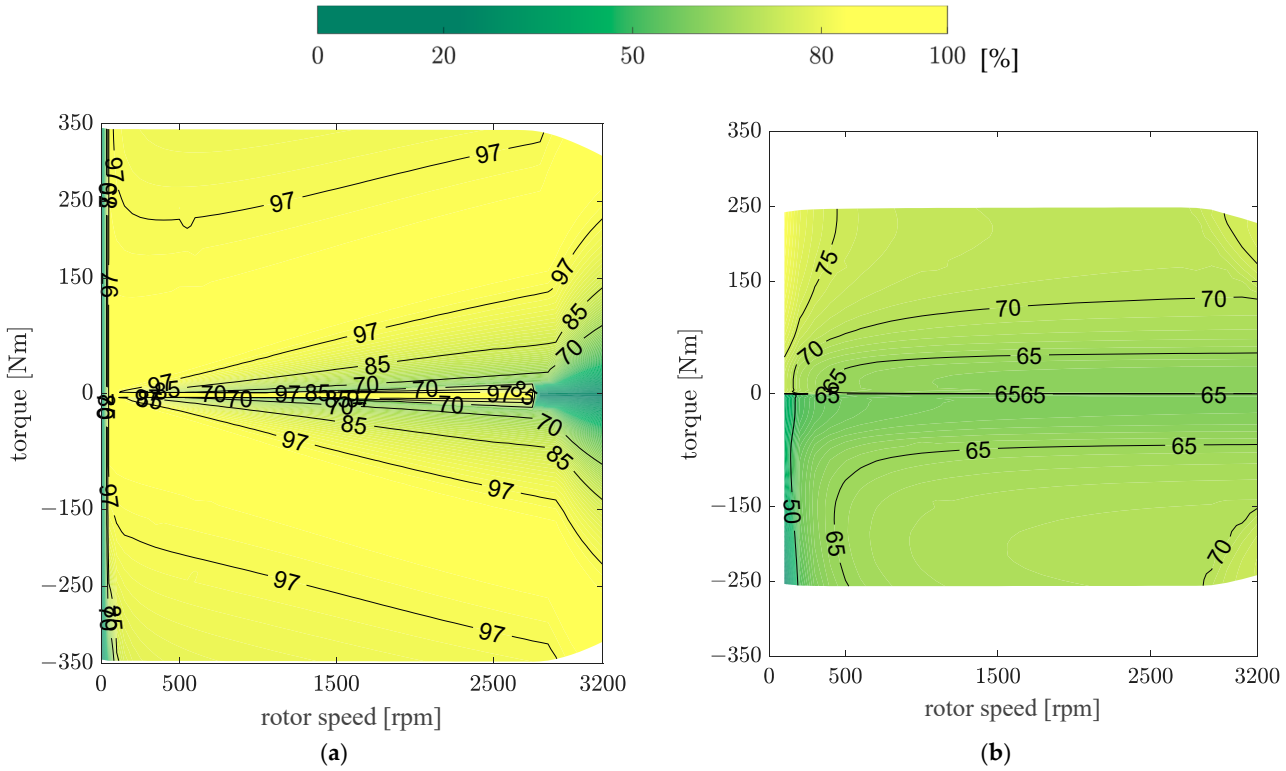

Figure 12. Two-dimensional FEA power factor results: (**a**) IPMSM, (**b**) IM.

5.2. Overload Condition

A transient temperature analysis is performed to examine the machine capability for handling 2 pu overload power for 30 s. It is assumed that the machines operate at the rated load (i.e., 345 Nm for IPMSM and 255 Nm for IM) and the rated speed of 2800 rpm from time t = 1 s to t = 1560 s. Then, a 2 pu load is applied for 30 s. After t = 1590 s, the machine continues its operation at full load for a further 610 s. The load torques for both machines are shown by the red lines in Figure 13a,b. Figure 13a shows the IPMSM temperature increased from 146 °C to 153 °C within 30 s, which is still within the limitation of the Class F insulation temperature (i.e., 155 °C). The transient temperature analysis of the IM, shown in Figure 13b, shows that the winding hotspot temperature changes from 114 °C to 152 °C during the overload operation. Thus, both machines have the capability of handling the required 2 pu overload.

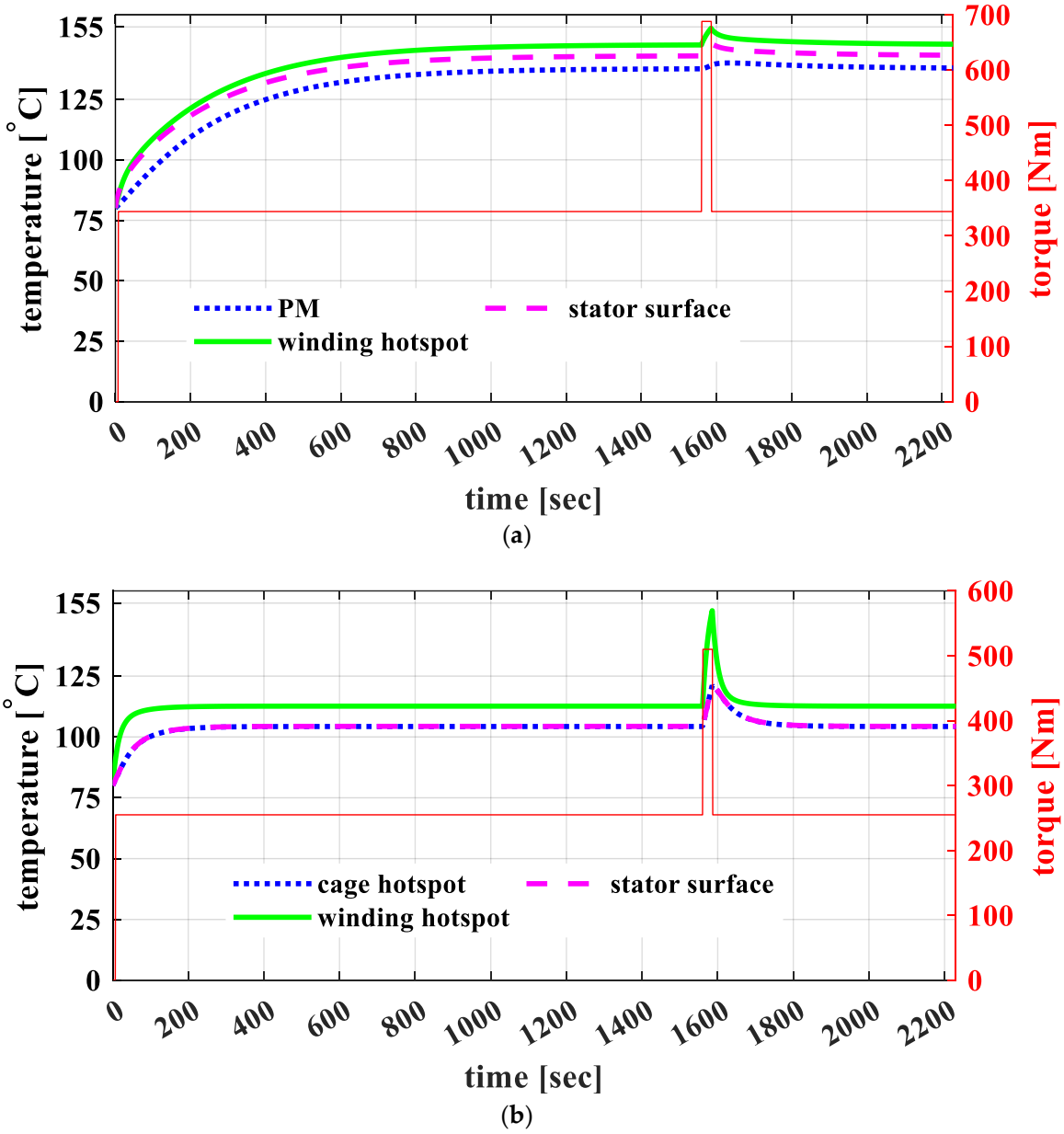

Figure 13. Three-dimensional FEA results of the transient thermal analysis of the designed machines: (**a**) IPMSM, (**b**) IM.

5.3. Number of Poles

This section describes a sensitivity analysis of the effect of the number of poles on the induction machine. Machines with 10 to 20 poles are considered while keeping the number of slots per pole per phase equal to 2. The output powers of the designed machines are compared with each other, taking into account the stator winding temperature limit.

The initial induction machine design used 12 poles and Figure 14 shows that increasing the number of poles results in lower output power because of the temperature limits. Increasing the number of poles results in a substantial increase in the core loss which is not offset by the small reduction in stator yoke thickness (see Figure 14b).

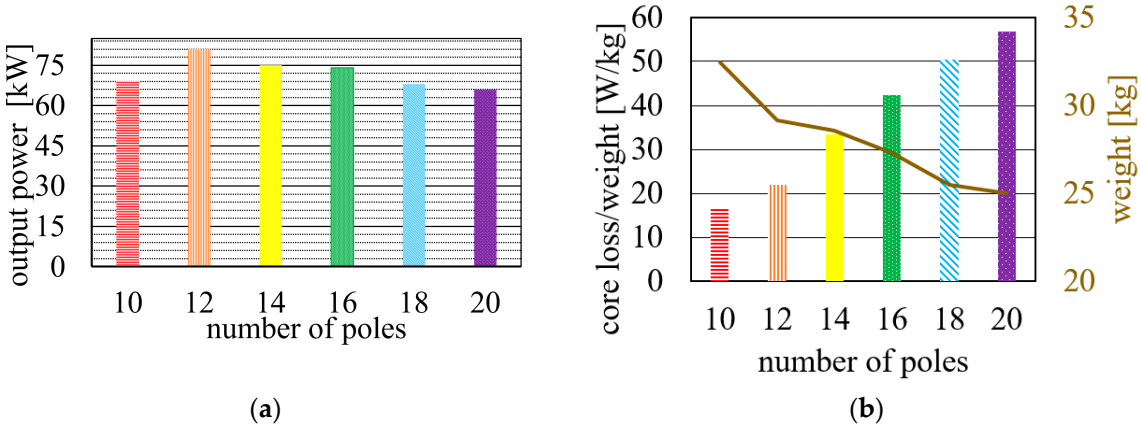

Figure 14. Two-dimensional FEA results of induction machines with different numbers of poles designed using the proposed process: (**a**) output power considering the thermal limit, (**b**) core loss/weight (bars) and weight (line).

5.4. Comparison of the Radial-Flux Designs with Axial-Flux Benchmarks

Given the tight axial length constraint of the traction application considered, axial-flux PM designs are an important alternative to the radial-flux PM and IM designs covered in this paper for this traction application. Thus, the performance parameters of the designed radial-flux machines are compared with four commercially available axial-flux designs and two axial-flux designs described in the literature, as shown in Table 6.

Table 6. Comparison of the performance parameters of the designed IPMSM and IM at 2800 rpm with four axial-flux designs available commercially and two from the literature. The reported values for the machines are taken from [15,45,59–62].

	Inlet Coolant Temperature	Max. Continuous Power	Max. Efficiency	Power Density
Proposed IPMSM	80 °C	103 kW	97%	2.08 kW/kg
Proposed IM	80 °C	75 kW	95%	1.43 kW/kg
eMobility IM [48]	65 °C	49.5 kW	93%	1.04 kW/kg
	80 °C	44.5 kW	≤93%	0.94 kW/kg
GVM210-100P [61]	60 °C	55 kW	-	1.57 kW/kg
	80 °C	48 kW	-	1.37 kW/kg
YASA-750 [62]	40 °C	70 kW	97%	1.89 kW/kg
	80 °C	49 kW	≤97%	1.32 kW/kg
EMRAX 268CC [63]	40 °C	105 kW	98%	5.12 kW/kg
	80 °C	60.8 kW	≤98%	2.96 kW/kg
AFPMSM [64]	80 °C	20 kW	91.5%	0.88 kW/kg
AFPMSM [15]	80 °C	82 kW	94%	2.3 kW/kg

The radial-flux IPMSM and IM designs use Class F insulation and, with the assumed 80 °C liquid coolant, are designed for operation at 130 °C during steady-state operation. The application requirement has a 2800 rpm rated speed. To provide a fair comparison, the output power of the benchmark machines is derated for this cooling arrangement and rated speed. Due to the limited information provided by the manufacturers, the following assumptions are made in the derating: the machines operate with a steady-state stator winding temperature of 130 °C and the available cooling is directly proportional to the difference between this and the coolant temperature; at this low speed only the copper loss

is considered and this loss is proportional to the square of current; and also the torque is proportional to current.

The induction machine described in Ref. [48] delivers 115 kW at a rated current and speed of 290 A and 6500 rpm with an inlet coolant of 65 °C. The output power of the machine is reduced to 49.5 kW at 2800 rpm. Considering a 15 °C higher temperature of the coolant, the amount of the loss should be reduced by 19%. Thus, the rated current will have a 10% reduction which produces a derated output power of 44.5 kW.

The Parker GVM210-100P [61] has a rated power of 106 kW with 60 °C coolant at 5373 rpm. Thus, this machine offers 55.2 kW output power at 2800 rpm with the 60 °C inlet coolant. The increase in the inlet temperature to 80 °C leads to a 13% reduction of the rated current and torque. Therefore, the derated output power of this machine drops to 48 kW with 80 °C coolant. Therefore, the power density of the machine is 1.37 kW/kg with respect to its 35 kg weight.

The YASA-750 is a commercial axial-flux PM machine which is rated at 70 kW and 3000 rpm with 40 °C coolant [62]. Using the above approximations, with 80 °C coolant, the derated output power is estimated at 49 kW at 2800 rpm.

The EMRAX 268CC [63] is another commercial axial-flux PM design and can deliver 105 kW at 4500 rpm with 50 °C coolant. The derated power for this machine is estimated at 60.8 kW at 2800 rpm.

Two different axial-flux PM synchronous machines (AFPMSMs) have been studied in the literature in Refs. [15,64]. The coolant inlet temperatures for the designed machines in Refs. [15,64] are 25 °C and 20 °C, respectively, and they have rated powers at 2800 rpm of 20 kW and 82 kW, respectively. The winding temperature in Ref. [64] at the rated current is 75 °C (i.e., the Class A insulation limit). If this insulation level is changed to Class F, the 45 °C increase in the inlet coolant temperature is compensated and no derating is required. This can also be applied to the machine in Ref. [15].

Table 6 summarizes the above results. It shows that the designed IPMSM and IM have promising performance and outperform some of the commercial designs, especially in output power and efficiency, with the relatively high inlet coolant temperature (80 °C), although the EMRAX 268CC remains superior in terms of power density. The designed IM also outperforms the eMobility IM and the GVM210-100P, which show significant reduction in continuous power and efficiency at higher temperatures. The YASA-750 demonstrates strong performance at a lower coolant temperature but has significant power derating when operating with 80 °C coolant. The two AFPMSM designs differ widely in performance, with one of the designs offering competitive power density and efficiency at 80 °C.

Note that the efficiency values for the designed IPMSM and IM do not include bearing/windage losses. Also, the power density shown does not include the housing, shaft, bearings etc. unlike the commercial machines [62,63] and the AFPMSM in Ref. [64]. The reported weight in Ref. [15] also does not cover the housing, shaft, and bearing weights.

6. Conclusions

A step-by-step design procedure for the design of interior permanent magnet synchronous machines (IPMSMs) and induction machines (IMs) for electric traction applications was proposed in this paper. A 100 kW direct-drive electric machine for a hybrid electric vehicle (HEV) was considered as the case study. An IPMSM and an IM were both designed for the HEV, and their performances were compared.

As the main contribution, this study incorporates both electromagnetic and thermal analyses to optimize the machine performance under normal and overload conditions and to provide insights into thermal limits. The effect of using different rotor magnet V angles in the IPMSM was studied and the advantages of using embedded magnets were described. It was found that the deep PM structure (V-60) offers the best electromagnetic performance parameters. Future work could include studying structural, noise, and vibration analysis for the considered designs to find the most suitable structure for high-power density IPMSMs.

The sensitivity of the performance of the induction machine to the number of rotor bars was examined to highlight the importance of this value. The effect of the selection of the pole number was another subject of the study. It was demonstrated that although it is expected to increase the power density by increasing the number of poles, the stator winding temperature limit can prevent reaching larger torques/higher power.

The comparison of the IPMSM and IM designs with the performance of four commercial designs and two designs from the literature showed the developed designs are competitive in power density and efficiency and can be used as a baseline for further optimization. For instance, optimization can be conducted by changing the slot widths and depths or PM dimensions as studied in various works from the literature. It should be highlighted that the expected performance parameters of the designed machines can be confirmed after construction and testing, which is the subject of future study.

Author Contributions: Conceptualization, E.R., A.M., W.L.S., S.K. and N.K.; methodology, E.R.; software, E.R.; validation, E.R., A.M., W.L.S., S.K. and N.K.; formal analysis, E.R., A.M., W.L.S. and S.K.; investigation, E.R.; resources, A.M.; data curation, E.R.; writing—original draft preparation, E.R.; writing—review and editing, A.M., W.L.S. and S.K.; visualization, A.M., W.L.S. and S.K.; supervision, A.M., W.L.S. and S.K.; project administration, A.M.; funding acquisition, A.M., S.K. and N.K. All authors have read and agreed to the published version of the manuscript.

Funding: This research was funded by Sovereign Propulsion Systems Pty Ltd., Adelaide, Australia.

Institutional Review Board Statement: Not applicable.

Informed Consent Statement: Not applicable.

Data Availability Statement: The original contributions presented in the study are included in the article, further inquiries can be directed to the corresponding authors.

Conflicts of Interest: Author Nathan Kalisch was employed by the company Sovereign Propulsion Systems. The remaining authors declare that the research was conducted in the absence of any commercial or financial relationships that could be construed as a potential conflict of interest. The sponsors had no role in the design, execution, interpretation, or writing of the study.

References

1. Roshandel, E.; Mahmoudi, A.; Soong, W.L.; Kahourzade, S. Optimal Design of Induction Motors Over Driving Cycles for Electric Vehicles. *IEEE Trans. Veh. Technol.* **2023**, *72*, 15548–15562. [CrossRef]
2. Qu, R.; Lipo, T.A. Sizing Equations and Power Density Evaluation of Dual-Rotor, Radial-Flux, Toroidally Wound, Permanent-Magnet Machines. *IEEE Trans. Ind. Appl.* **2004**, *39*, 1665–1673.
3. Roshandel, E.; Mahmoudi, A.; Kahourzade, S.; Soong, W.L. Saturation Consideration in Modeling of the Induction Machine Using Subdomain Technique to Predict Performance. *IEEE Trans. Ind. Appl.* **2022**, *58*, 261–272. [CrossRef]
4. Mahmoudi, A.; Kahourzade, S.; Roshandel, E.; Soong, W.L. Axial-Flux Synchronous Reluctance Motors: Introduction of a New Machine. In Proceedings of the 2020 IEEE International Conference on Power Electronics, Drives and Energy Systems (PEDES), Jaipur, India, 16–19 December 2020; pp. 1–6.
5. Ionel, D.M.; Popescu, M. Finite-element surrogate model for electric machines with revolving field-application to IPM motors. *IEEE Trans. Ind. Appl.* **2010**, *46*, 2424–2433. [CrossRef]
6. Kahourzade, S.; Mahmoudi, A.; Roshandel, E.; Cao, Z. Optimal design of Axial-Flux Induction Motors based on an improved analytical model. *Energy* **2021**, *237*, 121552. [CrossRef]
7. Eroglu, I.; Horlbeck, L.; Lienkamp, M.; Hackl, C.M. Increasing the overall efficiency of induction motors for BEV by using the overload potential through downsizing. In Proceedings of the 2017 IEEE International Electric Machines and Drives Conference (IEMDC), Miami, FL, USA, 21–24 May 2017. [CrossRef]
8. Hannon, B.; Sergeant, P.; Dupré, L. 2-D Analytical Subdomain Model of a Slotted PMSM with Shielding Cylinder. *IEEE Trans. Magn.* **2014**, *50*, 8101410. [CrossRef]
9. Djelloul-Khedda, Z.; Boughrara, K.; Ibtiouen, R.; Dubas, F. NonLinear analytical calculation of magnetic field and torque of switched reluctance machines. In Proceedings of the 2016 International Conference on Electrical Sciences and Technologies in Maghreb (CISTEM), Marrakech & Bengrir, Morocco, 26–28 October 2016; Volume 53. [CrossRef]
10. Roshandel, E.; Mahmoudi, A.; Kahourzade, S.; Soong, W. Analytical Model and Performance Prediction of Induction Motors using Subdomain Technique. In Proceedings of the 2020 IEEE Energy Conversion Congress and Exposition (ECCE), Detroit, MI, USA, 11–15 October 2020; pp. 3815–3822.

11. Tong, W.; Wang, S.; Dai, S.; Wu, S.; Tang, R. A quasi-three-dimensional magnetic equivalent circuit model of a double-sided axial flux permanent magnet machine considering local saturation. *IEEE Trans. Energy Convers.* **2018**, *33*, 2163–2173. [CrossRef]
12. Amrhein, M.; Krein, P.T. Induction machine modeling approach based on 3-D magnetic equivalent circuit framework. *IEEE Trans. Energy Convers.* **2010**, *25*, 339–347. [CrossRef]
13. Tak, B.O.; Ro, J.S. Analysis and design of an axial flux permanent magnet motor for in-wheel system using a novel analytical method combined with a numerical method. *IEEE Access* **2020**, *8*, 203994–204011. [CrossRef]
14. Lu, C.; Ferrari, S.; Pellegrino, G. Two Design Procedures for PM Synchronous Machines for Electric Powertrains. *IEEE Trans. Transp. Electrif.* **2017**, *3*, 98–107. [CrossRef]
15. Lai, J.; Li, J.; Xiao, T. Design of a Compact Axial Flux Permanent Magnet Machine for Hybrid Electric Vehicle. *IEEE Trans. Ind. Electron.* **2021**, *68*, 6630–6639. [CrossRef]
16. Du, J.; Wang, X.; Lv, H. Optimization of Magnet Shape Based on Efficiency Map of IPMSM for EVs. *IEEE Trans. Appl. Supercond.* **2016**, *26*, 0609807. [CrossRef]
17. Jung, H.-C.; Park, G.-J.; Kim, D.-J.; Jung, S.-Y. Optimal design and validation of IPMSM for maximum efficiency distribution compatible to energy consumption areas of HD-EV. *IEEE Trans. Magn.* **2017**, *53*, 8201904. [CrossRef]
18. Son, J.C.; Kim, J.Y.; Choi, J.W.; Lim, D.K.; Yeo, H.K. Performance Enhancement of the IPMSM for HEV Applications Using Grain-Oriented Electrical Steel and Design Optimization. *IEEE Access* **2022**, *10*, 46599–46607. [CrossRef]
19. Wang, L.; Tang, Z.; Zhang, P.; Liu, X.; Wang, D.; Li, X. Double Extended Sliding-Mode Observer-Based Synchronous Estimation of Total Inertia and Load Torque for PMSM-driven Spindle-Tool Systems. *IEEE Trans. Ind. Inform.* **2023**, *19*, 8496–8507. [CrossRef]
20. Chen, H.; Lee, C.H.T. Parametric Sensitivity Analysis and Design Optimization of an Interior Permanent Magnet Synchronous Motor. *IEEE Access* **2019**, *7*, 159918–159929. [CrossRef]
21. Min, S.G.; Sarlioglu, B. Analysis and Comparative Study of Flux Weakening Capability in Fractional-Slot Concentrated Windings. *IEEE Trans. Energy Convers.* **2018**, *33*, 1025–1035. [CrossRef]
22. Choi, G.; Bramerdorfer, G. Comprehensive Design and Analysis of an Interior Permanent Magnet Synchronous Machine for Light-Duty Passenger EVs. *IEEE Access* **2022**, *10*, 819–831. [CrossRef]
23. Yang, Y.; Castano, S.M.; Yang, R.; Kasprzak, M.; Bilgin, B.; Sathyan, A.; Dadkhah, H.; Emadi, A. Design and Comparison of Interior Permanent Magnet Motor Topologies for Traction Applications. *IEEE Trans. Transp. Electrif.* **2017**, *3*, 86–97. [CrossRef]
24. Liu, X.; Chen, H.; Zhao, J.; Belahcen, A. Research on the Performances and Parameters of Interior PMSM Used for Electric Vehicles. *IEEE Trans. Ind. Electron.* **2016**, *63*, 3533–3545. [CrossRef]
25. Zhang, Y.; Cao, W.; McLoone, S.; Morrow, J. Design and Flux-Weakening Control of an Interior Permanent Magnet Synchronous Motor for Electric Vehicles. *IEEE Trans. Appl. Supercond.* **2016**, *26*, 0606906. [CrossRef]
26. Kim, K.C.; Kim, K.; Kim, H.J.; Lee, J. Demagnetization analysis of permanent magnets according to rotor types of interior permanent magnet synchronous motor. *IEEE Trans. Magn.* **2009**, *45*, 2799–2802. [CrossRef]
27. Gao, P.; Sun, X.; Gerada, D.; Gerada, C.; Wang, X. Improved V-shaped interior permanent magnet rotor topology with inward-extended bridges for reduced torque ripple. *IET Electr. Power Appl.* **2020**, *14*, 2404–2411. [CrossRef]
28. Wang, S.-C.; Nien, Y.-C.; Huang, S.-M. Multi-Objective Optimization Design and Analysis of V-Shape Permanent Magnet Synchronous Motor. *Energies* **2022**, *15*, 3496. [CrossRef]
29. Chakraborty, S.; Nair, S.V.; Hatua, K. Effect of v Angle Variation and Strengthening Rib on Performance Characteristics of IPMSM Motor for Electric Vehicles. In Proceedings of the 2021 1st International Conference on Power Electronics and Energy (ICPEE), Bhubaneswar, India, 2–3 January 2021. [CrossRef]
30. Joksimović, G.; Levi, E.; Kajević, A.; Mezzarobba, M.; Tessarolo, A. Optimal Selection of Rotor Bar Number for Minimizing Torque and Current Pulsations Due to Rotor Slot Harmonics in Three-Phase Cage Induction Motors. *IEEE Access* **2020**, *8*, 228572–228585. [CrossRef]
31. Mahmoudi, A.; Roshandel, E.; Kahourzade, S.; Soong, W.L. Line-Start Permanent-Magnet Synchronous Motor: Axial-Flux vs Radial-Flux Configuration. In Proceedings of the 2023 IEEE International Conference on Energy Technologies for Future Grids (ETFG), Wollongong, Australia, 3–6 December 2023; pp. 1–6.
32. Tao, F.; Jian, L.; Xuhui, W.; Xiaofeng, L. A new sizing equation and it's application in electrical machine design. In Proceedings of the 2011 International Conference on Electric Information and Control Engineering, Wuhan, China, 15–17 April 2011; pp. 3890–3893.
33. Zhang, D.; Park, C.S.; Koh, C.S. A new optimal design method of rotor slot of three-phase squirrel cage induction motor for NEMA class D speed-torque characteristic using multi-objective optimization algorithm. *IEEE Trans. Magn.* **2012**, *48*, 879–882. [CrossRef]
34. To, T.T.; Roshandel, E.; Mahmoudi, A.; Cao, Z.; Kahourzade, S. Optimization of IM Rotor Bars Inclination Angle using Analytical Model in Free FEA Software. In Proceedings of the 2021 IEEE Energy Conversion Congress and Exposition (ECCE), Vancouver, BC, Canada, 10–14 October 2021; pp. 4119–4126.
35. Dianati, B.; Kahourzade, S.; Mahmoudi, A. Optimization of Axial-Flux Induction Motors for the Application of Electric Vehicles Considering Driving Cycles. *IEEE Trans. Energy Convers.* **2020**, *35*, 1522–1533. [CrossRef]
36. Pao-La-Or, P.; Peaiyoung, S.; Kulworawanichpong, T.; Sujitjorn, S. Effects of the Geometry of the Rotor Slots on the Mechanical Vibration of Three-phase Induction Motors. In Proceedings of the 7th WSEAS International Conference on Simulation, Modelling and Optimization, Beijing, China, 15–17 September 2007; pp. 434–438.

37. Akhtar, M.J.; Behera, R.K.; Parida, S.K. Optimized rotor slot shape for squirrel cage induction motor in electric propulsion application. In Proceedings of the 2014 IEEE 6th India International Conference on Power Electronics (IICPE), Kurukshetra, India, 8–10 December 2014; pp. 1–5.
38. Lordoglu, A.; Gulbahce, M.O.; Kocabas, D.A. A comprehensive disturbing effect analysis of multi-sectional rotor slot geometry for induction machines in electrical vehicles. *IEEE Access* **2021**, *9*, 49590–49600. [CrossRef]
39. Hasegawa, Y.; Nakamura, K.; Ichinokura, O. Optimization of a Switched Reluctance Motor Made of Permendur. *IEEE Trans. Magn.* **2010**, *46*, 1311–1314. [CrossRef]
40. Hao, Z.; Zhou, W.; Ji, T.; Huang, X.; Zhang, C. Multi-Objective Optimization of Double Primary Tubular Permanent Magnet Synchronous Linear Motor in Wide Temperature Range Environment Based on Pareto Front Method. *IEEE Access* **2020**, *8*, 207193–207203. [CrossRef]
41. Roshandel, E.; Mahmoudi, A.; Soong, W.L.; Kahourzade, S.; Lei, G.; Guo, Y.; Kalisch, N. Design of a 100 kW Axial Flux Permanent Magnet Direct Drive Machine for a Hybrid Electric Vehicle. In Proceedings of the 2022 32nd Australasian Universities Power Engineering Conference, AUPEC 2022, Adelaide, Australia, 26–28 September 2022.
42. Gai, Y.; Kimiabeigi, M.; Chuan Chong, Y.; Widmer, J.D.; Deng, X.; Popescu, M.; Goss, J.; Staton, D.A.; Steven, A. Cooling of automotive traction motors: Schemes, examples, and computation methods. *IEEE Trans. Ind. Electron.* **2019**, *66*, 1681–1692. [CrossRef]
43. Zhou, K.; Pries, J.; Hofmann, H. Computationally Efficient 3-D Finite-Element-Based Dynamic Thermal Models of Electric Machines. *IEEE Trans. Transp. Electrif.* **2015**, *1*, 138–149. [CrossRef]
44. Ansys Motor-CAD. Electric Machine Design Software. 2021. Available online: https://www.ansys.com/products/electronics/ansys-motor-cad (accessed on 3 September 2023).
45. Roshandel, E.; Mahmoudi, A.; Kahourzade, S.; Soong, W.L. Design and Analysis of Small Aspect-Ratio Switched Reluctance Motor. In Proceedings of the 2020 IEEE International Conference on Power Electronics, Drives and Energy Systems (PEDES), Jaipur, India, 16–19 December 2020; pp. 1–6.
46. Yang, X.; Fatemi, A.; Nehl, T.; Hao, L.; Zeng, W.; Parrish, S. Comparative Study of Three Stator Cooling Jackets for Electric Machine of Mild Hybrid Vehicle. *IEEE Trans. Ind. Appl.* **2021**, *57*, 1193–1201. [CrossRef]
47. Roshandel, E.; Mahmoudi, A.; Kahourzade, S.; Yazdani, A.; Shafiullah, G.M. Losses in efficiency maps of electric vehicles: An overview. *Energies* **2021**, *14*, 7805. [CrossRef]
48. Flaherty, N. Radial Flux Motors. E-Mobility Engineering. Available online: https://www.emobility-engineering.com/radial-flux-motors/ (accessed on 3 September 2023).
49. Boubaker, N.; Matt, D.; Enrici, P.; Nierlich, F.; Durand, G. Measurements of iron loss in PMSM stator cores based on CoFe and SiFe lamination sheets and stemmed from different manufacturing processes. *IEEE Trans. Magn.* **2019**, *55*, 8100309. [CrossRef]
50. Zhu, Z.Q.; Xue, S.; Chu, W.; Feng, J.; Guo, S.; Chen, Z.; Peng, J. Evaluation of Iron Loss Models in Electrical Machines. *IEEE Trans. Ind. Appl.* **2019**, *55*, 1461–1472. [CrossRef]
51. Rao, J.; Gao, Y.; Li, D.; Qu, R. Performance Analysis of Interior Permanent Magnet Motor Using Overlapping Windings with Fractional Ratio of Slot to Pole Pair. *IEEE Trans. Appl. Supercond.* **2016**, *26*, 0610005. [CrossRef]
52. Kiyota, K.; Chiba, A. Design of switched reluctance motor competitive to 60-kW IPMSM in third-generation hybrid electric vehicle. *IEEE Trans. Ind. Appl.* **2012**, *48*, 2303–2309. [CrossRef]
53. Jeong, M.-J.; Lee, K.-B.; Song, S.-W.; Lee, S.-H.; Kim, W.-H. A Study on Magnetization Yoke Design for Post-Assembly Magnetization Performance Improvement of a Spoke-Type Permanent Magnet Synchronous Motor. *Machines* **2023**, *11*, 850. [CrossRef]
54. Gieras, J.F. *Permanent Magnet Motor Technology: Design and Applications*; CRC Press: Boca Raton, FL, USA, 2002; ISBN 0824743946.
55. Soltani, M.; Nuzzo, S.; Barater, D.; Franceschini, G. A Multi-Objective Design Optimization for a Permanent Magnet Synchronous Machine with Hairpin Winding Intended for Transport Applications. *Electronics* **2021**, *10*, 3162. [CrossRef]
56. Chin, J.-W.; Cha, K.-S.; Park, M.-R.; Park, S.-H.; Lee, E.-C.; Lim, M.-S. High Efficiency PMSM With High Slot Fill Factor Coil for Heavy-Duty EV Traction Considering AC Resistance. *IEEE Trans. Energy Convers.* **2021**, *36*, 883–894. [CrossRef]
57. Farahani, M.; Gockenbach, E.; Borsi, H.; Schäfer, K.; Kaufhold, M. Behavior of machine insulation systems subjected to accelerated thermal aging test. *IEEE Trans. Dielectr. Electr. Insul.* **2010**, *17*, 1364–1372. [CrossRef]
58. Joksimovic, G.; Kajevic, A.; Mezzarobba, M.; Tessarolo, A. Optimal rotor bars number in four pole cage induction motor with 36 stator slots—Part II: Results. In Proceedings of the 2020 International Conference on Electrical Machines (ICEM), Gothenburg, Sweden, 23–26 August 2020; pp. 509–514. [CrossRef]
59. Thomas, R.; Garbuio, L.; Gerbaud, L.; Chazal, H. Modeling and design analysis of the Tesla Model S induction motor. In Proceedings of the 2020 International Conference on Electrical Machines (ICEM), Gothenburg, Sweden, 23–26 August 2020; Volume 1, pp. 495–501.
60. Roshandel, E.; Mahmoudi, A.; Kahourzade, S.; Soong, W.L. Efficiency Maps of Electrical Machines: A Tutorial Review. *IEEE Trans. Ind. Appl.* **2023**, *59*, 1263–1272. [CrossRef]
61. Global Vehicle Motor. PARKER GVM210-100 ELECTRIC VEHICLE AC TRACTION MOTOR 350 VDC. Available online: https://www.elmofo.com.au/parker-gvm210-400-350.html (accessed on 3 September 2023).
62. Yasa Motor. YASA. Available online: https://yasa.com/technology/ (accessed on 3 September 2023).

63. EMRAX. Manual for EMRAX Motors/Generators. 2020. Available online: https://emrax.com/wp-content/uploads/2020/03/manual_for_emrax_motors_version_5.4.pdf (accessed on 3 September 2023).
64. Chang, J.; Wang, C. Electromagnetic thermal coupling analysis for a novel cooling system of an axial flux hub motor. *IET Electr. Power Appl.* **2022**, *16*, 421–433. [CrossRef]